Journal of Power Sources 629 (2025) 235861

Contents lists available at ScienceDirect

Journal of Power Sources

journal homepage: www.elsevier.com/locate/jpowsour

Superior electrochemical performance and reduced heat generation in 3D printed vs. 2D tape-casted NMC622 electrodes

Yucheng Zhou [a], Asya Orhan [b], Jianchao Ye [b], Nicolas Leport [a], Marcus A. Worsley [b], Laurent Pilon [a,c,d,*]

[a] Mechanical and Aerospace Engineering Department, Henry Samueli School of Engineering and Applied Science, University of California, Los Angeles, CA 90095, USA
[b] Materials Science Division, Lawrence Livermore National Laboratory, 7000 East Ave, Livermore, CA 94550, USA
[c] California NanoSystems Institute, University of California, Los Angeles, CA 90095, USA
[d] Institute of the Environment and Sustainability, University of California, Los Angeles, CA 90095, USA

GRAPHICAL ABSTRACT

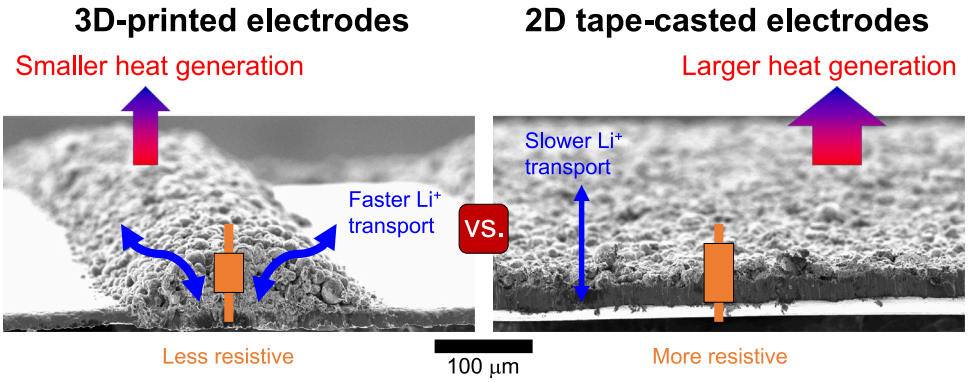

HIGHLIGHTS

- Electrodes with NMC622 ribbon lines were fabricated by a novel 3D-printing process.
- Conventional 2D tape-casted NMC622 electrodes were also produced for comparison.
- The two types of electrodes had similar open-circuit voltage and entropic potential.
- 3D-printed electrodes showed superior specific capacity and rate performance.
- 3D-printed electrodes featured lower electrical energy loss and heat generation.

ARTICLE INFO

Keywords:
Lithium-ion battery
Additive manufacturing
Entropic potential
Galvanostatic intermittent titration technique
Calorimetry

ABSTRACT

This study compares the charge storage mechanisms, thermodynamics behavior, ion transport, and heat generation in NMC622 electrodes fabricated using a novel 3D printing process and the conventional 2D tape casting process. First, potentiometric entropy measurements revealed that the charge storage mechanisms for both types of electrodes consisted of lithium deintercalation in a homogeneous solid solution of NMC622 followed by a transition from a hexagonal (H1) phase to another hexagonal (H2) phase through a monoclinic

* Corresponding author at: Mechanical and Aerospace Engineering Department, Henry Samueli School of Engineering and Applied Science, University of California, Los Angeles, CA 90095, USA.
E-mail address: pilon@seas.ucla.edu (L. Pilon).

https://doi.org/10.1016/j.jpowsour.2024.235861
Received 31 August 2024; Received in revised form 11 November 2024; Accepted 13 November 2024
Available online 4 December 2024

Thermal management

(M) phase. Both types of electrodes had similar thermodynamics behavior with overlapping entropic potential profiles. Furthermore, *operando* isothermal calorimetry at high C-rates indicated that the 3D printed electrodes featured larger specific capacity and better rate performance than the 2D tape-casted electrodes. The better performance of 3D printed electrodes was attributed to their larger electrode/electrolyte interfacial surface area and electrical conductivity as well as their faster lithium ion transport. As a result, the instantaneous heat generation rates were smaller in 3D printed electrodes than in 2D tape-casted electrodes, thus resulting in lower overall specific electrical energy and thermal energy dissipation per unit charge stored. Overall, additive manufacturing techniques offer great potential in producing electrodes with superior electrochemical performance and reduced heat generation for fast charging batteries.

1. Introduction

Electrical energy storage systems such as lithium-ion batteries [1–6] and supercapacitors [7–12] have come to the fore as essential components in enabling the electrification and decarbonization of transportation. Research and development efforts have focused on the improvement of energy and power densities and on the fabrication of electrodes which combine excellent gravimetric and volumetric capacity as well as favorable rate performance during fast charging [13–16]. Therefore, both the equilibrium electrochemical charge storage capability and fast ion transport have to be accounted for when designing and manufacturing electrodes [17–21].

Additive manufacturing techniques, such as three-dimensional (3D) printing, have been introduced as a fabrication process of electrodes with optimum morphology. Multiple approaches have been proposed including (i) mixed printing of active materials, (ii) mixed printing of precursors, and (iii) active materials deposited on printed aerogels [22]. Specifically, 3D printed electrodes made of materials such as lithium iron phosphate (LFP), lithium titanium oxide (LTO) [23], graphene oxide (GO) [24], and manganese oxide (MnO_2) [25] have generally demonstrated superior rate capability than their counterparts fabricated by conventional slurry casting techniques. The origins of these performance advantages can be traced to two principal factors [21,22,26–28]. First, the increased electrode/electrolyte interfacial surface area of a properly designed 3D printed electrode provides more sites for physicochemical activity such as redox reactions and electrical double layer formation. Second, the topology of a properly designed 3D printed electrode can reduce the electronic and ionic diffusion resistances while facilitating the accessibility of the electrolyte to the bulk of the electrode active materials. However, although the electrochemical behavior of various 3D printed electrodes has been illustrated in several studies [23–25], the thermodynamics behavior and the heat generation rates of such electrodes have not been investigated.

Our previous study [29] compared slurry-casted electrodes made of $Ti_2Nb_2O_9$ microparticles (around 1 μm) or $Ti_2Nb_2O_9$ nanoparticles (around 50 nm) using state-of-the-art potentiometric entropy measurements and *operando* isothermal calorimetry [29–32]. We showed that both types of electrodes had similar thermodynamics behavior due to their identical chemical composition. However, electrodes made of $Ti_2Nb_2O_9$ nanoparticles exhibited not only superior electrochemical performance but also reduced heat generation rates compared to those made of microparticles. This difference was attributed to the enhanced reaction kinetics and ion transport within $Ti_2Nb_2O_9$ nanoparticles compared to microparticles.

The present study aims to compare the thermodynamics behavior and the heat generation rates in 3D printed electrodes with those in conventional slurry-casted electrodes made with the same lithium manganese nickel cobalt oxide $LiNi_{0.6}Mn_{0.2}Co_{0.2}O_2$ (NMC622) slurry. This compound was chosen because it has been widely adopted as a cathode material in commercial batteries for not only its stability but also its large specific capacity and rate performance [33,34]. This study can provide insight into the energy losses and heat dissipation mechanisms in 3D printed electrodes, particularly during fast charging.

2. Background

2.1. Additive manufacturing techniques for electrode fabrication

2.1.1. 3D printing of active material mixtures

In recent years, substantial attention has been paid to applications of novel additive manufacturing techniques such as 3D printing in the electrode fabrication process, with rapid progress in multiple areas for different anode, cathode, and pseudocapacitive materials [22]. The first approach consists of printing a mixture of active materials. For example, Fu et al. [23] produced inks for 3D printing of electrodes where the raw materials consisted of lithium iron phosphate (LFP) or lithium titanium oxide (LTO) mixed with graphene oxide (GO). The corresponding ink viscoelasticity was optimized for extrusion-based fabrication. The resulting 3D printed electrodes exhibited promising specific capacity, rate performance, and cycling stability. In a similar study, Drews et al. [35] presented a silicon/graphite blend slurry designed for 3D printed electrodes of interdigitated microbatteries, which also recorded excellent cycling performance. Moreover, Zhao et al. [36] described a fabrication method of graphene-based composite aerogel microlattices built upon 3D printing. In fact, graphene/ZnV_2O_6@$Co_3V_2O_8$ and graphene/vanadium nitride (VN) electrodes prepared according to the porous microlattice structure achieved superior energy and power densities than other conventionally fabricated pseudocapacitive electrodes. Finally, Zhu et al. [37] proposed a direct ink writing procedure utilizing concentrated inks featuring low electrical resistivity, submillimeter particle size, and high mechanical stability. The process was used to produce a 1 mm-thick zinc electrode with sizeable areal and volumetric capacity without significant microstructural degradation during long-term cycling.

2.1.2. 3D printing of precursor material mixtures

3D printing can also be performed using a mixture of precursor materials. For instance, Zhu et al. [24] created a mixture containing graphene oxide (GO) precursor to form graphene composite aerogel electrodes with a composite microlattice structure. These electrodes displayed excellent capacity even under high currents and power densities comparable to 10 times thinner slurry-casted electrodes. Similarly, Yao et al. [38] prepared a 3D printing ink by combining cellulose nanocrystals (CNC) and a silica microsphere suspension. The resulting multiscale porous carbon aerogel electrodes achieved capacitance of 149 F/g at 5 mV/s and 71 F/g at 200 mV/s when tested at −70 °C. These capacitance values were 6.5 times higher than slurry-casted electrodes. In contrast to these pseudocapacitive electrodes, Idrees et al. [39] proposed a novel porous carbon (PC)/silicon oxycarbide (SiOC) composite for 3D printing into anodes for zinc-ion batteries. Thanks to the interpenetrated SiOC network within the PC, the electrodes enjoyed not only improved transport properties but also uniform nucleation of zinc ions within the voids. As a result, the superior capacity of the electrodes was accompanied by significantly reduced dendrite formation, thus extending their cycle life. In the case of sodium-ion batteries, Brown et al. [40] demonstrated a 3D printing ink consisting of ammonium thiomolybdate mixed with graphene oxide (GO) nanosheets. This produced MoS_2-graphene aerogel electrodes with excellent specific capacity along with fast and highly reversible sodium ion transport. As such, when utilized as anodes for sodium-ion batteries these samples showed outstanding rate performance and cycling stability.

2.1.3. Deposition of active materials on 3D printed aerogels

Another 3D printing technique relies on depositing active materials on separately 3D printed and patterned aerogels to generate the desired electrodes for different types of supercapacitor or battery chemistries. Yao et al. [25,41] demonstrated (i) cathodes made of 3D printed graphene aerogels with high mass loading of deposited MnO_2 and (ii) anodes made of 3D printed graphene aerogels with high density of surface functional groups. When paired together, the full supercapacitor device achieved excellent energy and power densities, where the primary charge storage mechanism came from redox reactions with fast kinetic processes. More recently, Lin et al. [42] manufactured 3D printed graphene aerogels with both sparsely separated exterior ligaments to create large open channels for mass transport and densely arranged interior ligaments to provide large ion-accessible active surface. Similar approaches have been used to produce (i) sulfur cathodes in lithium-sulfur batteries [43], (ii) lithium anodes in lithium-lithium iron phosphate (LFP) batteries [44], (iii) sodium anodes in sodium-ion batteries [45], and (iv) zinc anodes in zinc-ion batteries [46]. In general, the controlled deposition of active materials on intricately designed 3D printed hosts not only enabled high mass loading and excellent transport kinetics but also mitigated dendrite formation by virtue of the more uniform ion nucleation on the electrode/electrolyte interface.

2.1.4. 3D printing of NMC materials

For the NMC group of materials akin to the NMC622 investigated in the present study, there have been previous attempts to utilize 3D printing. Martinez et al. [47] employed a vat photopolymerization precursor procedure to synthesize NMC111 electrodes with complex shapes and submicron features which maintained adequate mechanical rigidity. Tao et al. [48] used a conformal heat-drying direct ink writing process to produce NMC811 electrodes with enhanced rate performance (144 mAh/g at 3C) and cycling stability (60% capacity recovered after 800 cycles at 1C). The rising number of experimental studies featuring 3D printed electrodes has also prompted several numerical modeling efforts [26–28]. These studies sought to quantitatively elucidate the reasons of performance enhancement obtained with additive manufacturing techniques in order to propose design rules and optimization strategies.

2.2. Potentiometric entropy measurements

The theoretical backgrounds for potentiometric entropy measurements have been described in detail in our previous studies and need not be repeated [29–32]. In brief, potentiometric entropy measurements consist of determining the open-circuit voltage $U_{OCV}(x,T)$ and the entropic potential $\partial U_{OCV}(x,T)/\partial T$ of a battery cell at a specified temperature T and pressure as functions of lithium composition x. The evolution of both $U_{OCV}(x,T)$ and $\partial U_{OCV}(x,T)/\partial T$ can offer insight into the charge storage mechanisms of the battery cell including lithium ion insertion in a homogeneous solid solution, two-phase coexistence, phase transition, and intralayer lithium ion ordering [49].

In addition, the apparent diffusion coefficient $D_{Li^+}(x,T)$ of lithium ions in the NMC622 working electrode can be estimated from the transient behavior of the cell potential during galvanostatic intermittent titration technique (GITT) measurements based on Fick's second law of diffusion such that [50],

$$D_{Li^+}(x,T) = -\left(\frac{L_{NMC}}{\pi}\right)^2 \frac{\mathrm{d}\log[V(x,T,t) - U_{OCV}(x,T)]}{\mathrm{d}t}. \quad (1)$$

Here, L_{NMC} is the thickness of the NMC622 working electrode, $V(x,T,t)$ is the recorded cell potential during the relaxation period after a given current pulse, and $U_{OCV}(x,T)$ is the equilibrium open-circuit voltage retrieved at the end of that particular relaxation period.

2.3. Heat generation in batteries

Here also, our previous studies [29–32] have presented the derivations and interpretations of different heat generation mechanisms in batteries. In summary, the instantaneous total heat generation rate $\dot{Q}_T(x,T)$ (in W) in a battery cell can be divided into the following contributions: (i) Joule heating $\dot{Q}_J(x,T)$, (ii) reversible entropic heat generation $\dot{Q}_{rev}(x,T)$, (iii) enthalpy of mixing $\dot{Q}_{mix}(x,T)$, and (iv) heat generation due to side reactions $\dot{Q}_{sr}(x,T)$, i.e. [51–54],

$$\dot{Q}_T(x,T) = \dot{Q}_J(x,T) + \dot{Q}_{rev}(x,T) + \dot{Q}_{mix}(x,T) + \dot{Q}_{sr}(x,T). \quad (2)$$

Any given heat generation rate $\dot{Q}_i(x,T)$ is positive (or negative) when the corresponding phenomenon is exothermic (or endothermic) and release (or absorb) heat. First, the Joule heating term $\dot{Q}_J(x,T)$ arising from irreversible resistive losses can be expressed as [51–54],

$$\dot{Q}_J(x,T) = I[V(x,T) - U^{avg}(x,T)] \approx I[V(x,T) - U_{OCV}(x,T)]. \quad (3)$$

Here, I is the imposed current, $V(x,T)$ is the cell potential, and $U^{avg}(x,T)$ is equivalent to the open-circuit voltage $U_{OCV}(x,T)$ retrieved from potentiometric entropy measurements, with the overpotential $[V(x,T) - U^{avg}(x,T)]$ defined as the potential drop across the cell due to internal resistance. Furthermore, the reversible term $\dot{Q}_{rev}(x,T)$ associated with entropic changes can be expressed as [51–54],

$$\dot{Q}_{rev}(x,T) = IT\frac{\partial U^{avg}(x,T)}{\partial T} \approx IT\frac{\partial U_{OCV}(x,T)}{\partial T}. \quad (4)$$

In addition, the term attributed to enthalpy of mixing $\dot{Q}_{mix}(x,T)$ is dominated by the effect of ion concentration gradients (i) across the electrolyte due to diffusion limitations, (ii) across the electrode due to non-uniform current distribution, (iii) within the pores of the electrode filled with electrolyte, and (iv) among intercalated lithium ions in the electrode due to electrochemical reactions [51,52,55]. Finally, the term due to side reactions $\dot{Q}_{sr}(x,T)$ was neglected in this study since the battery cell was pristine and operating under moderate conditions [51,53,54,56].

The net thermal energy Q_i (in J) resulting from each individual contribution and released over a charging/discharging cycle can be expressed as [54],

$$Q_i = \oint_{cycle} \dot{Q}_i(x,T,t)\mathrm{d}t \quad \text{with } i = T,\ J,\ \text{or } mix. \quad (5)$$

Note that the reversible heat generation rate $\dot{Q}_{rev}(x,T,t)$ averages to zero over a cycle, i.e., $Q_{rev} = 0$. Similarly, the net electrical energy loss ΔE_e (in J) over a charging/discharging cycle corresponds to the area enclosed by the hysteresis of $V(x,T)$ vs. the charge transferred q such that [57],

$$\Delta E_e = \oint_{cycle} V(x,T)\mathrm{d}q = \oint_{cycle} V(x,T,t)I(t)\mathrm{d}t. \quad (6)$$

Based on the first law of thermodynamics, the total thermal energy released during a cycle is equal to the net electrical energy loss, i.e. [29–32],

$$\Delta E_e = Q_T = Q_J + Q_{mix}. \quad (7)$$

3. Materials and methods

3.1. Electrode and device fabrication

In this study, 3D printed NMC622 electrodes were prepared using an ink consisting of NMC622 powder (Targray), conductive carbon (Super C65 Carbon Black Conductive Additive, MSE Pro), and polyvinylidene fluoride (Solef 5140 PVDF, Solvay) with a mass ratio of 90:5:5. Here, both NMC622 and conductive carbon powders were ground with mortar and pestle before being added to a solution of 8 wt% PVDF in N-methyl-2-pyrrolidone (NMP) solvent. The final solvent content of the

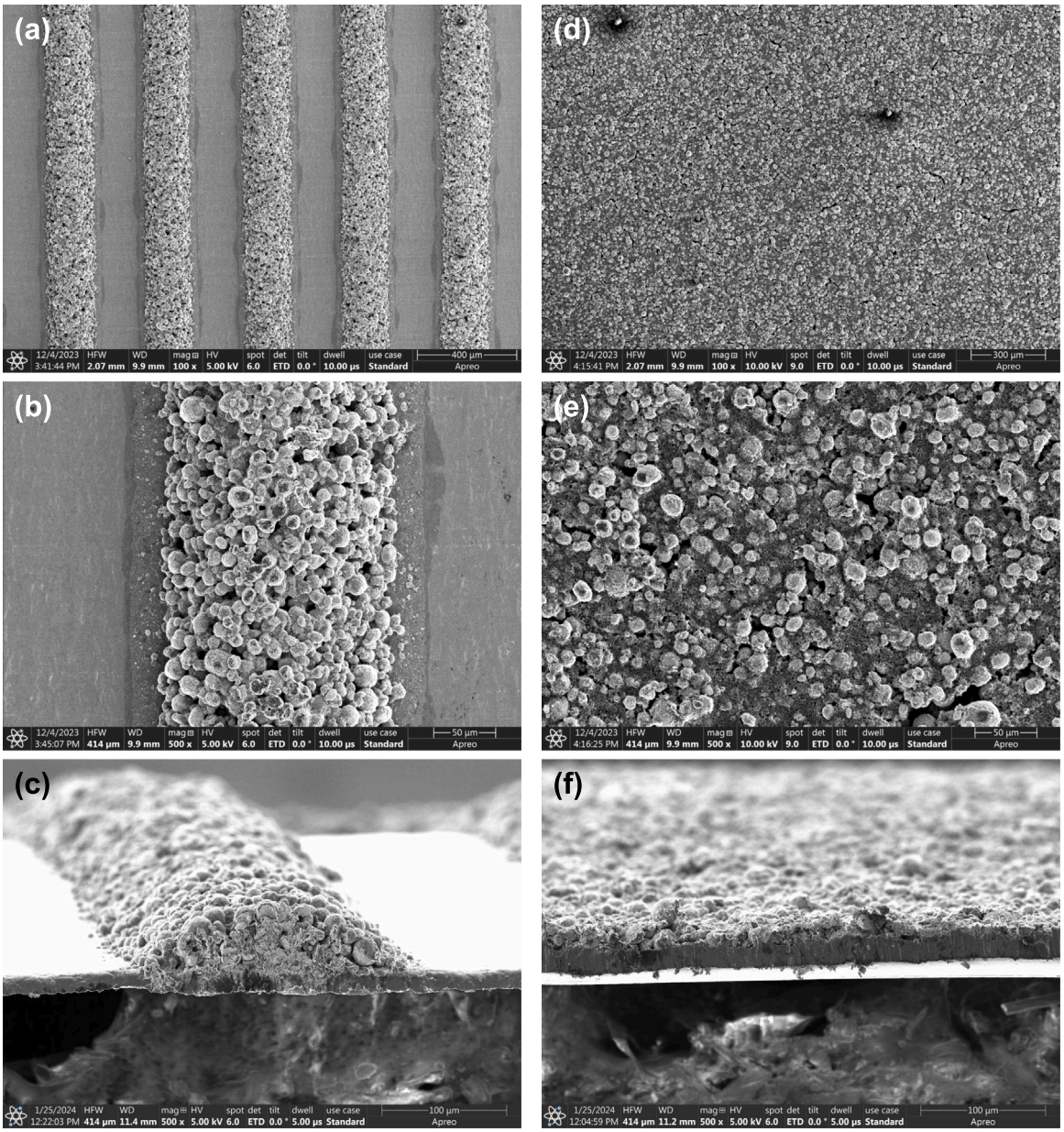

Fig. 1. Scanning electron microscopy (SEM) images of (a, b, c) 3D printed or (d, e, f) 2D tape-casted NMC622 electrodes with the broad view, the top view, and the cross-sectional view, respectively.

slurry was 29 wt%. The slurry was then filtered using a stainless steel 300 × 300 mesh with 0.0021-inch opening size before being printed on an aluminum foil current collector using a Hyrel 3D printer (Engine High Resolution). Specifically, 10 mm × 10 mm squares with zig-zag line patterns were printed with nozzle diameter of 0.2 mm, speed of 180 mm/min, and hatch spacing of 0.4 mm, resulting in electrodes with an active material mass loading around 5 mg/cm^2.

As a reference, 2D tape-casted NMC622 electrodes were prepared with the same procedure, except that additional NMP solvent was added to the slurry for a final solvent content of 58 wt% to facilitate uniform casting. Then, the slurry was casted using a tape caster with thickness of 150 μm to obtain electrodes with an active material mass loading also around 5 mg/cm^2. Finally, both 3D printed and 2D tape-casted NMC622 electrodes were dried in a vacuum oven at 80 °C overnight. The approximately uniform thickness of the 2D tape-casted electrodes was around 34 μm.

One set of each type of electrodes was cut using a 0.5-inch diameter hole punch to assemble CR2032 coin cells for potentiometric entropy measurements. Here, the coin cells consisted of (i) a 3D printed or a 2D tape-casted NMC622 working electrode, (ii) lithium metal (MTI, 99.9%) as the counter electrode (250 μm thickness, 16 mm diameter), (iii) a 25 μm thick PP-PE-PP trilayer microporous membrane (Celgard 2325) as the separator, and (iv) 1.2 M $LiPF_6$ in EC:EMC 3:7 w/w (Soulbrain MI) electrolyte. Note that two pieces of 500 μm thick stainless steel spacers and one wave spring were used in the cell assembly. The coin cells were assembled in a glove box containing Ar gas with less than 0.5 ppm of O_2 and H_2O.

Another set of each type of electrodes was cut into 1 cm × 1 cm square to be used in *operando* isothermal calorimetry. Here, the so-called calorimetric cells consisted of (i) a 3D printed or a 2D tape-casted NMC622 working electrode, (ii) a 1 cm × 1 cm polished lithium metal (Sigma Aldrich, 99.9%) piece 750 μm in thickness serving as the counter electrode, (iii) a 670 μm thick glass microfiber filter sheet (Whatman GF/D) acting as the separator and thermal insulator, and (iv) 1.2 M $LiPF_6$ in EC:EMC 3:7 w/w (Soulbrain MI) electrolyte. The calorimetric

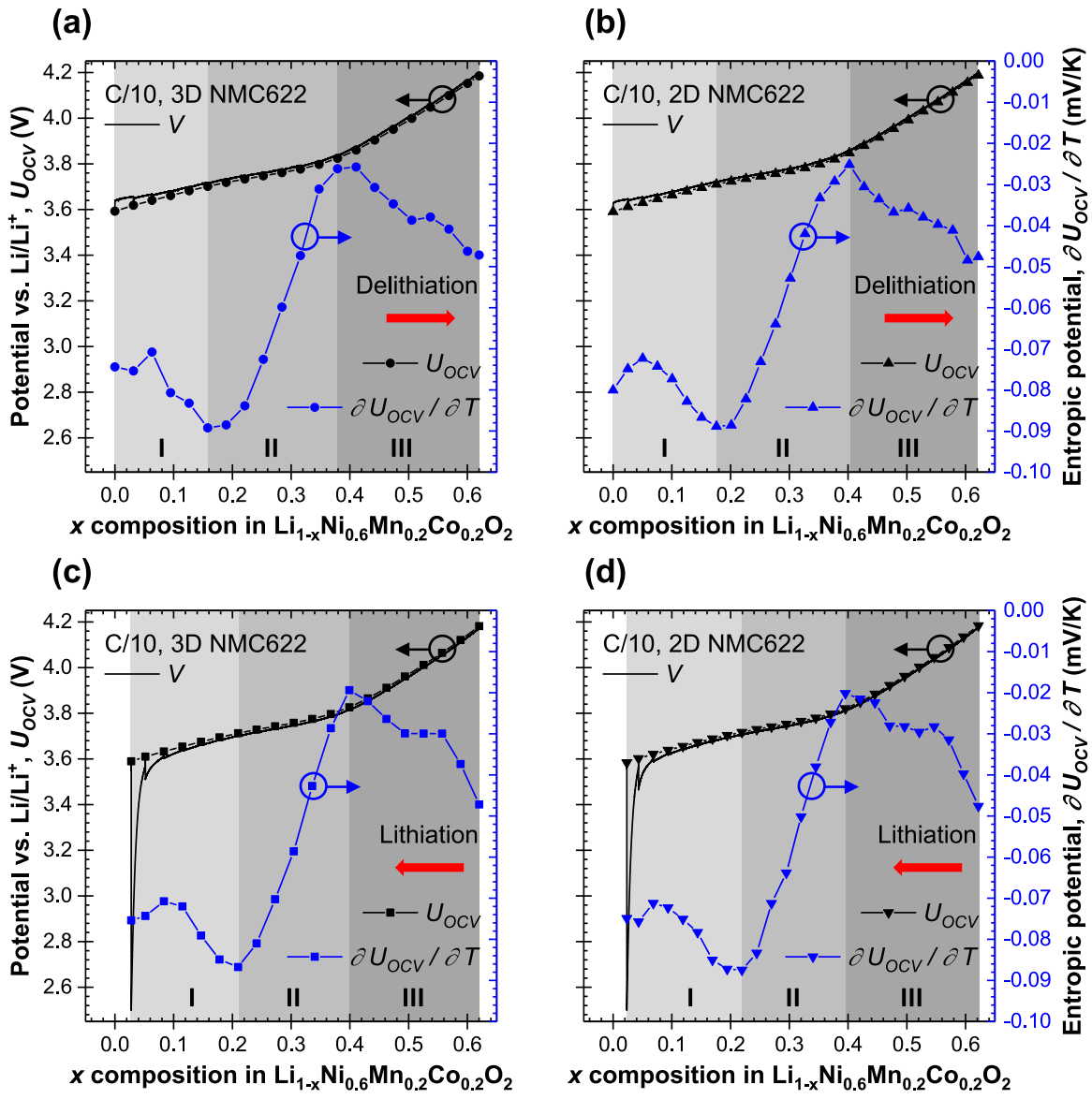

Fig. 2. Cell potential $V(x,T)$, open-circuit voltage $U_{OCV}(x,T)$, and entropic potential $\partial U_{OCV}(x,T)/\partial T$ of coin cells with working electrodes made of 3D printed or 2D tape-casted NMC622 as functions of lithium composition x during delithiation and lithiation at C-rate of C/10.

cells were also assembled in a glove box containing Ar gas with less than 0.5 ppm of O_2 and H_2O.

3.2. Potentiometric entropy measurements and operando isothermal calori metry

Potentiometric entropy measurements and *operando* isothermal cal orimetry followed the same procedures as those described in our previous studies [29–32]. For potentiometric entropy measurements, a series of constant current pulses was imposed to the coin cell corresponding to a C-rate of C/10 at 20 °C. Each current pulse lasted 30 min followed by a relaxation period of 270 min. Towards the end of each relaxation period, a step-like temperature profile was applied to the coin cell from 15 °C to 25 °C in 5 °C increments with a thermoelectric cold plate (TE technology, CP-121). The corresponding coin cell potential evolution was simultaneously recorded by a high accuracy potentiostat (BioLogic, VSP-300).

For *operando* isothermal calorimetry, galvanostatic cycling was imposed to the calorimetric cell using a high accuracy potentiostat (BioLogic, SP-150). The instantaneous heat generation rates at the working electrode made of 3D printed or 2D tape-casted NMC622 and at the lithium metal counter electrode were measured simultaneously using 1 cm × 1 cm thermoelectric heat flux sensors (greenTEG, gSKIN-XP) in thermal contact with the back of each electrode. Note that the calorimeter operated under isothermal conditions and the thermal mass of the electrodes were small so that the electrode temperature was uniform and constant over time despite heat generation.

Finally, note that the recorded cell potential $V(t)$ under galvanostatic cycling at constant current $\pm I$ exhibits a so-called IR drop denoted as ΔV when switching between charging and discharging or vice versa. Then, the internal resistance R_{GC} of the cell was calculated according to [58–62],

$$R_{GC} = \frac{\Delta V}{2I}. \tag{8}$$

4. Results and discussion

4.1. Electrode morphology

Fig. 1 shows the scanning electron microscopy (SEM) images of (a, b, c) 3D printed or (d, e, f) 2D tape-casted NMC622 electrodes with the

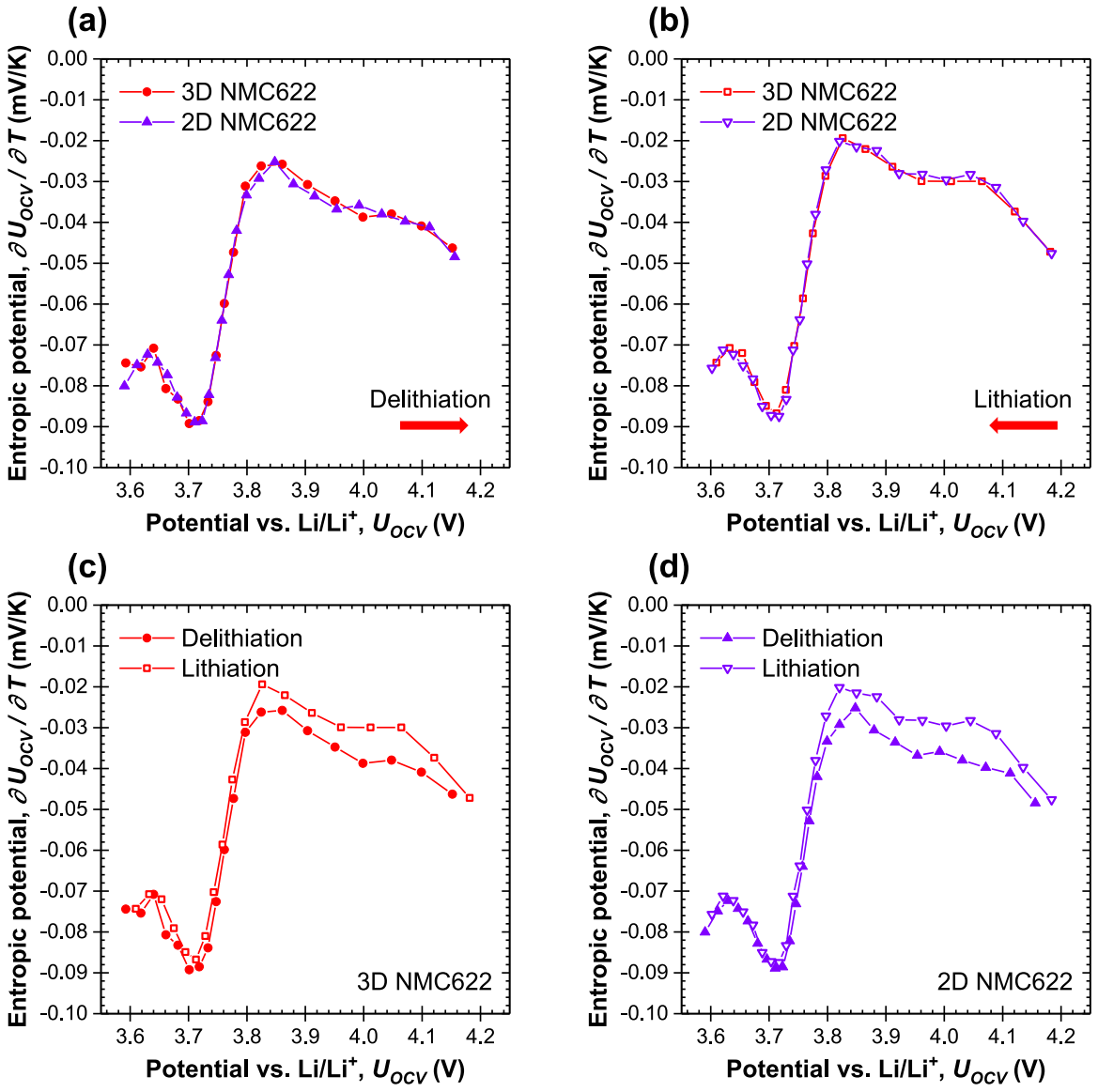

Fig. 3. Entropic potential $\partial U_{OCV}(x,T)/\partial T$ of coin cells as a function of open-circuit voltage $U_{OCV}(x,T)$ during delithiation and lithiation at C-rate of C/10 for working electrodes made of 3D printed or 2D tape-casted NMC622.

broad view, the top view, and the cross-sectional view, respectively. Every ribbon line of the 3D printed electrodes had an average width of 240 μm and an average height of 50 μm, while the 2D tape-casted electrodes had an approximately uniform thickness of 34 μm. Both types of electrodes were laid on an aluminum foil current collector around 15 μm in thickness. Here, we assume that the material in both types of electrodes had identical porosity and effective density. In addition, the cross-sectional geometry of the 3D printed electrodes is modeled as a parabola with a width of 240 μm and a height of 50 μm, while the 2D tape-casted electrodes have a rectangular cross-section with a height of 34 μm equal to the electrode thickness. Finally, the length perpendicular to the cross-section is also the same between both types of electrodes. Overall, calculated according to these geometries, the 3D printed electrodes had nearly 15% larger exterior surface area exposed to the electrolyte per unit volume of the bulk electrode than the 2D tape-casted electrodes. It was also observed that the NMC622 particles in the 3D printed electrodes were more concentrated in the outer than in the inner region of the ribbon lines, as established from the varying textures in Fig. 1(c). By contrast, for the 2D tape-casted electrodes shown in Fig. 1(f), the NMC622 particles were more homogeneously distributed. As a result, the 3D printed electrodes featured reduced diffusion length required to reach the NMC622 particles, which could improve the utilization rate of the NMC622 active materials, particularly under faster cycling conditions.

4.2. Potentiometric entropy measurements

Fig. 2 plots the cell potential $V(x,T)$, open-circuit voltage $U_{OCV}(x,T)$, and entropic potential $\partial U_{OCV}(x,T)/\partial T$ of the coin cells with working electrodes made of (a, c) 3D printed or (b, d) 2D tape-casted NMC622 as functions of lithium composition x during (a, b) delithiation and (c, d) lithiation at C-rate of C/10. Here, the NMC622 mass loading of the 3D printed and 2D tape-casted NMC622 electrodes was 4.7 and 5.4 mg/cm^2, respectively. First, within the same potential window from 2.5 to 4.2 V vs. Li/Li$^+$, the range of lithium composition x was almost identical between the two cells, i.e., $0 < x < 0.6$. This corresponds to a specific capacity of 166 mAh/g consistent with that reported in other studies [33,34].

Furthermore, the similar evolutions of $U_{OCV}(x,T)$ and $\partial U_{OCV}(x,T)/\partial T$ for both cells indicate the same charge storage mechanisms during both delithiation and lithiation. In Region I ($0 < x < 0.2$), $U_{OCV}(x,T)$ increased monotonously and $\partial U_{OCV}(x,T)/\partial T$

mostly decreased corresponding to lithium deintercalation in a homogeneous solid solution [49]. A similar behavior was observed in Region III ($0.4 < x < 0.6$), where the increasing $U_{OCV}(x,T)$ and the decreasing $\partial U_{OCV}(x,T)/\partial T$ were again associated with lithium ion deinsertion in a homogeneous solid solution [49]. Finally, in the intermediate Region II ($0.2 < x < 0.4$), $U_{OCV}(x,T)$ increased with a reduced slope while $\partial U_{OCV}(x,T)/\partial T$ increased rapidly. Interestingly, Region II coincided with the so-called transition from a hexagonal (H1) phase (Region I) to another hexagonal (H2) phase (Region III) through a monoclinic (M) phase, as described in Ref. [34]. In contrast to a typical transformation between two fundamentally distinct phases, here the transition only caused a minor increase in the c lattice parameter of NMC622 during delithiation. This resulted in a slight gliding between adjunct transition metal-oxygen layers and a slight repulsion of neighboring oxygen layers [34]. Nevertheless, this structural distortion likely shifted the configurational entropy which in turn resulted in an increase in $\partial U_{OCV}(x,T)/\partial T$ [49].

Fig. 3 plots the entropic potential $\partial U_{OCV}(x,T)/\partial T$ of the coin cells as a function of open-circuit voltage $U_{OCV}(x,T)$ during (a) delithiation and (b) lithiation at C-rate of C/10 for working electrodes made of (c) 3D printed or (d) 2D tape-casted NMC622. This so-called entropic potential profile, first proposed by Hudak et al. [63], enables a direct comparison between the thermodynamics behavior of different cells. In fact, this profile eliminates interferences from factors such as specific capacity differences, lithiation/delithiation hysteresis, and specific capacity loss from trapped lithium ions and/or increasing kinetic barriers over cycles. Here, Figs. 3(a) and 3(b) indicate that the entropic potential profiles of both cells overlapped with negligible discrepancy during both delithiation and lithiation. In addition, Figs. 3(c) and 3(d) establish that the entropic potential profiles of both types of NMC622 electrodes were highly reversible between delithiation and lithiation. Only minor hysteresis existed at potentials above 3.8 V previously identified as Region III and associated with lithium deintercalation within the H2 phase.

The GITT procedure as part of potentiometric entropy measurements can also inform transport phenomena within the cells. First, it is evident from Fig. 2 that both cells exhibited very small overpotential $[V(x,T) - U_{OCV}(x,T)]$ and very small hysteresis in $U_{OCV}(x,T)$. Fig. 4 plots the apparent diffusion coefficient $D_{Li^+}(x,T)$ of lithium ions in the working electrodes made of 3D printed or 2D tape-casted NMC622 during (a) delithiation and (b) lithiation calculated according to Eq. (1). It indicates that the rate of lithium ion transport in both samples was relatively consistent throughout the entire range of lithium composition x. Overall, the 3D printed NMC622 electrodes showed slightly less overpotential and slightly enhanced apparent diffusion coefficient compared to the 2D tape-casted NMC622 electrodes. In order to observe the effects of the larger electrical conductivity and/or faster lithium ion transport in 3D printed vs. 2D tape-casted NMC622 electrodes [64], the cells should to be tested under faster cycling conditions using *operando* isothermal calorimetry measurements.

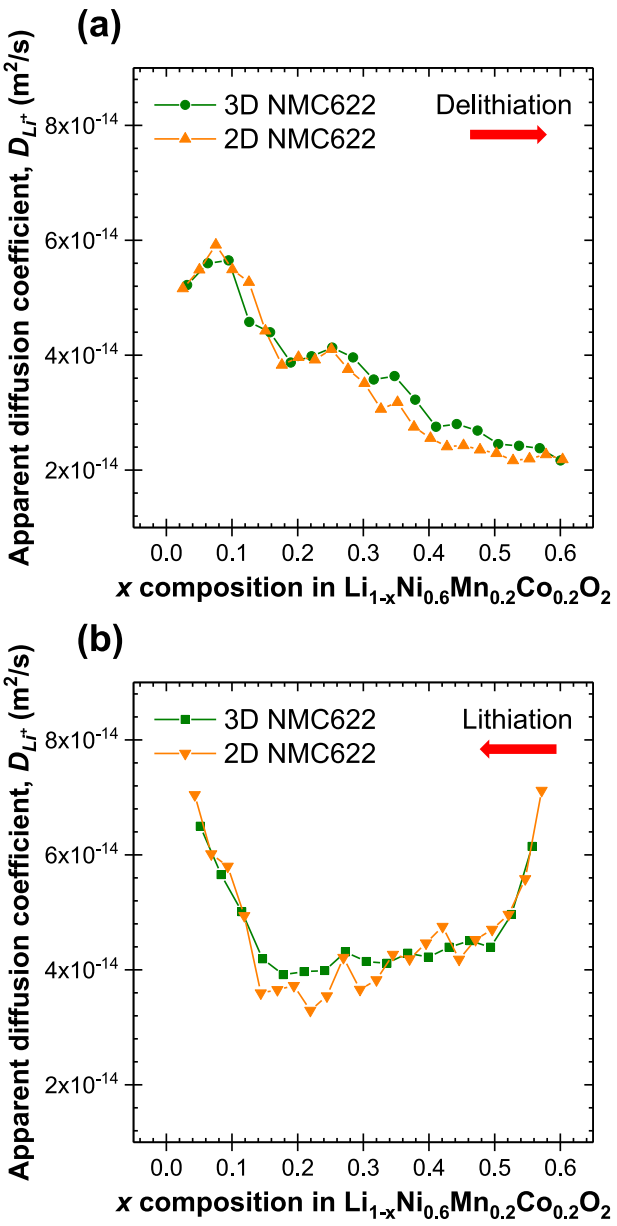

Fig. 4. Apparent diffusion coefficient $D_{Li^+}(x,T)$ [Eq. (1)] of lithium ions in the working electrodes made of 3D printed or 2D tape-casted NMC622 during (a) delithiation and (b) lithiation.

4.3. Operando isothermal calorimetry

4.3.1. Cell potential

Figure S1 in Supplementary Materials plots the temporal evolution of the potential $V(t)$ of the calorimetric cells with working electrodes made of (a) 3D printed or (b) 2D tape-casted NMC622 and lithium metal counter electrodes were subjected to galvanostatic cycling within the potential window from 1.7 to 5.0 V vs. Li/Li$^+$ at C-rates of 1C (around 0.8 mA/cm^2), 2C, and 3C. Although NMC622 is indeed a material with good rate performance compared to other cathode materials, an NMC622/lithium cell still typically shows visible capacity fade for C-rates exceeding 1C [65]. Therefore, the calorimetric cells were not tested at C-rates higher than 3C, as the specific capacity at higher C-rates would be too small to be relevant in practice. Note that this potential window was wider than that imposed in other measurements to account for the increased amount of overpotential observed in the calorimeter due to the thicker separator. Here, the NMC622 mass loading of the 3D printed and 2D tape-casted NMC622 electrodes was 4.3 and 5.0 mg/cm^2, respectively. Each colored region in Figure S1 corresponded to the five consecutive galvanostatic cycles at each of the C-rates considered. It shows that the potential $V(t)$ of both cells was nonlinear, asymmetric between charging and discharging, and repeatable at any given C-rate except for the first formation cycle. The duration of charging or discharging half-cycles were denoted respectively by t_c or t_d [Figure S1(c)]. Higher C-rates led not only to faster charging and discharging rates but also to smaller specific capacity. Moreover, the cycle period $t_{cd} = t_c + t_d$ and thus the specific capacity of the cell with the 3D printed NMC622 electrode was longer than that with the 2D tape-casted NMC622 electrode and did not decrease as much with increasing C-rate. Figure S1(d) compares the specific capacity of charging or discharging half-cycles, denoted respectively by $C_{m,c}$ or $C_{m,d}$, for the two cells at various C-rates. It reveals the superior

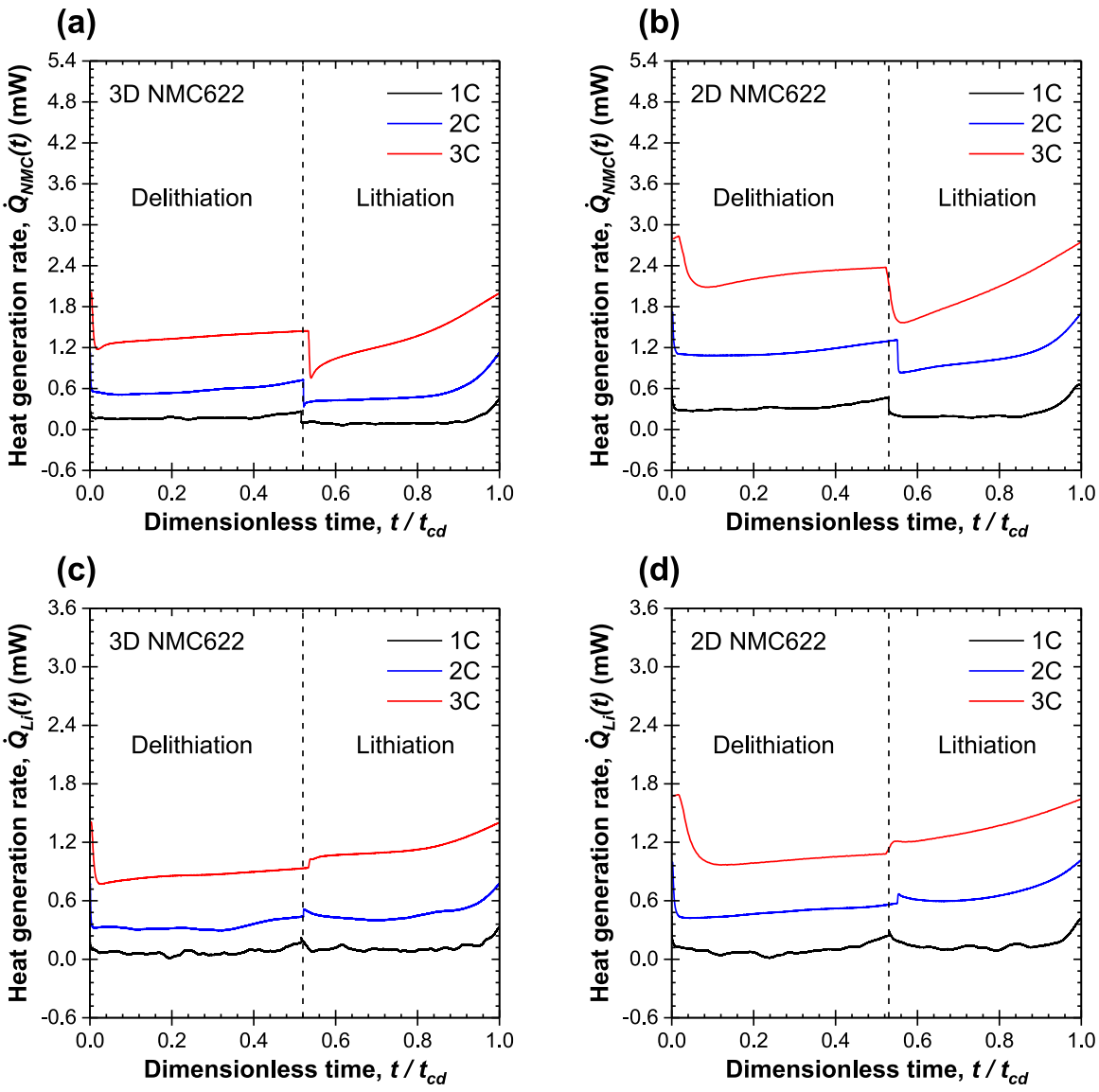

Fig. 5. Instantaneous heat generation rates (a, b) $\dot{Q}_{NMC}(t)$ measured at the working electrodes made of 3D printed or 2D tape-casted NMC622 with similar mass loading and (c, d) $\dot{Q}_{Li}(t)$ measured at the respective lithium metal counter electrodes as functions of dimensionless time t/t_{cd} averaged over the last three consecutive cycles at C-rates of 1C, 2C, and 3C.

rate performance of the 3D printed NMC622 electrode. Note that the absolute values of capacity shown in Figure S1(d) is relatively small since the thicker separator serving as thermal insulation between the electrodes in the calorimetric measurements increased the total cell resistance and reduced the specific capacity compared to most other cell configurations.

4.3.2. Instantaneous heat generation rates

Fig. 5 plots the instantaneous heat generation rates (a, b) $\dot{Q}_{NMC}(t)$ measured at the working electrodes made of 3D printed or 2D tape-casted NMC622 and (c, d) $\dot{Q}_{Li}(t)$ measured at the respective lithium metal counter electrodes as functions of dimensionless time t/t_{cd} averaged over the last three consecutive cycles at C-rates of 1C, 2C, and 3C. Note that the measurements of $\dot{Q}_{NMC}(t)$ and $\dot{Q}_{Li}(t)$ were repeatable cycle after cycle. First, the magnitudes of $\dot{Q}_{NMC}(t)$ and $\dot{Q}_{Li}(t)$ in both cells followed similar temporal behavior and increased with increasing C-rate. More importantly, Figs. 5(a) and 5(b) indicate that, at any given C-rate, $\dot{Q}_{NMC}(t)$ was larger by nearly a factor of 2 at the working electrode made of 2D tape-casted NMC622 than at that made of 3D printed NMC622 with similar mass loading. Furthermore, $\dot{Q}_{NMC}(t)$ in both cells not only decreased at the start of delithiation but also increased towards the end of lithiation. This could be attributed to the increasing electrical resistivity of NMC622 with lithiation [33,34], resulting in increasing Joule heating.

Figs. 5(c) and 5(d) establish that the heat generation rate $\dot{Q}_{Li}(t)$ of the lithium metal counter electrode was nearly the same in either cell at any given C-rate. In addition, $\dot{Q}_{Li}(t)$ remained relatively constant during delithiation of NMC622. This could be attributed to the constant electrical resistivity of lithium metal [29,31,32] and the continuous process involving endothermic desolvation of lithium ions prior to the exothermic plating of the lithium metal counter electrode. By contrast, $\dot{Q}_{Li}(t)$ increased towards the end of lithiation of NMC622. This was possibly due to the onset of exothermic ion pairing [29,31,32] in addition to the endothermic lithium ion stripping followed by exothermic lithium ion solvation at the lithium metal counter electrode. The transition between the endothermic desolvation and the exothermic solvation events explained the upturn in $\dot{Q}_{Li}(t)$ when switching from delithiation to lithiation of NMC622, and vice versa. Similar phenomena were also observed in our previous studies with PNb_9O_{25} [31], $Ti_2Nb_2O_9$ [29], or $(W_{0.2}V_{0.8})_3O_7$ [32] working electrodes and lithium metal counter electrodes.

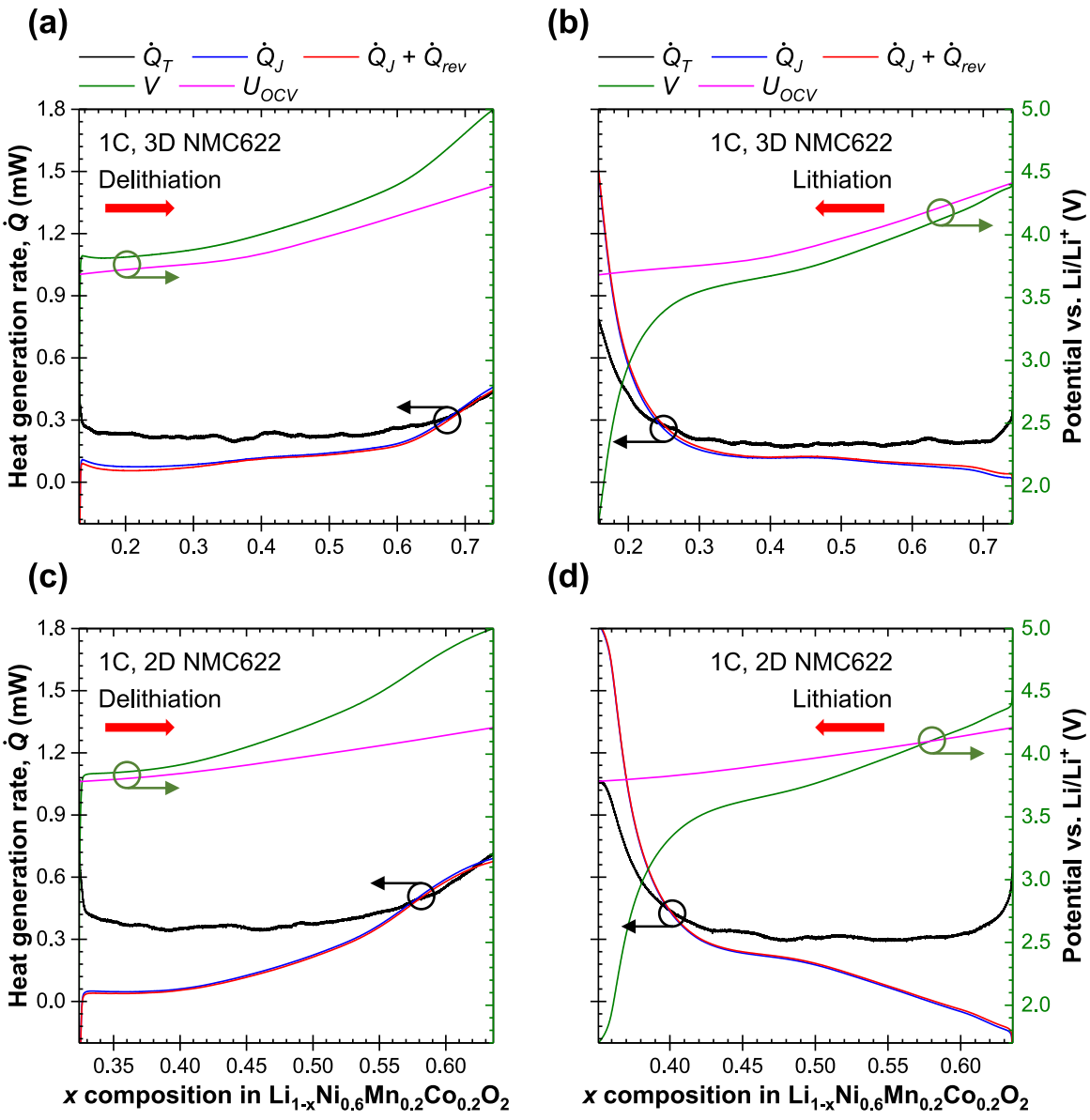

Fig. 6. Measured total heat generation rate $\dot{Q}_T(x,T)$, along with heat generation rates $\dot{Q}_J(x,T)$ and $\dot{Q}_J(x,T) + \dot{Q}_{rev}(x,T)$ calculated according to Eqs. (3) and (4), as well as measured cell potential $V(x,T)$ and open-circuit voltage $U_{OCV}(x,T)$ as functions of lithium composition x during delithiation and lithiation at C-rate of 1C in calorimetric cells with working electrodes made of 3D printed or 2D tape-casted NMC622 and lithium metal counter electrodes.

4.3.3. Total heat generation rate of the cell

Fig. 6 plots the measured total heat generation rate $\dot{Q}_T(x,T)$ in the calorimetric cells with working electrodes made of (a, b) 3D printed or (c, d) 2D tape-casted NMC622 and lithium metal counter electrodes as a function of lithium composition x during delithiation and lithiation at C-rate of 1C. Here, the measured cell potential $V(x,T)$ and open-circuit voltage $U_{OCV}(x,T)$ were also plotted. Figure S2 in Supplementary Materials shows that the overpotential $[V(x,T) - U_{OCV}(x,T)]$ was smaller in the cell with 3D printed NMC622 than that with 2D tape-casted NMC622. This demonstrates that, under such faster cycling conditions, the cell with 3D printed NMC622 achieved smaller internal resistance, which can be associated with smaller electrode/electrolyte interfacial resistance due to faster interfacial kinetics, as well as smaller mass transfer resistance due to faster lithium ion transport. Fig. 6 also shows the heat generation rates $\dot{Q}_J(x,T)$ and $\dot{Q}_J(x,T) + \dot{Q}_{rev}(x,T)$ predicted according to Eqs. (3) and (4). Note that the values of $U_{OCV}(x,T)$ and $\partial U_{OCV}(x,T)/\partial T$ previously determined by potentiometric entropy measurements (Fig. 2) were used as the values of $U^{avg}(x,T)$ and $\partial U^{avg}(x,T)/\partial T$ in these equations. Here, the measured total heat generation rate $\dot{Q}_T(x,T)$ agreed relatively well with the calculated heat generation rate $\dot{Q}_J(x,T) + \dot{Q}_{rev}(x,T)$. The contribution from Joule heating $\dot{Q}_J(x,T)$ was generally larger in the cell with 2D tape-casted NMC622 than that with 3D printed NMC622. In addition, in both cells $\dot{Q}_J(x,T)$ surged towards the end of lithiation due to the growing difference between $V(x,T)$ and $U_{OCV}(x,T)$ (Fig. 2). Moreover, the reversible entropic heat generation $\dot{Q}_{rev}(x,T)$ was endothermic during delithiation and exothermic during lithiation, since $\partial U_{OCV}(x,T)/\partial T$ always carried a negative value. Nevertheless, $\dot{Q}_{rev}(x,T)$ was found to be negligible compared to $\dot{Q}_J(x,T)$ which dominated heat generation. The difference between $\dot{Q}_T(x,T)$ and $\dot{Q}_J(x,T) + \dot{Q}_{rev}(x,T)$ originated from the irreversible exothermic enthalpy of mixing $\dot{Q}_{mix}(x,T)$ due to ion concentration gradients.

4.3.4. Time-averaged heat generation rates

Fig. 7(a) plots the time-averaged irreversible heat generation rates $\bar{\dot{Q}}_{irr,NMC}$ and $\bar{\dot{Q}}_{irr,Li}$ as functions of current I for calorimetric cells with

working electrodes made of 3D printed or 2D tape-casted NMC622. First, $\bar{Q}_{irr,NMC}$ and $\bar{Q}_{irr,Li}$ in both cells increased with increasing current I. Specifically, least squares fitting revealed that both $\bar{Q}_{irr,NMC}$ and $\bar{Q}_{irr,Li}$ increased quadratically with respect to current I, i.e., $\bar{Q}_{irr,NMC} \propto I^2$ and $\bar{Q}_{irr,Li} \propto I^2$. This suggests that in both cells Joule heating dominated the irreversible heat generation at both electrodes. Furthermore, for any given current I, $\bar{Q}_{irr,Li}$ was similar in both cells as observed in Figs. 5(c) and 5(d). Indeed, each lithium metal counter electrode was cut from the same piece into the same size and therefore should have approximately the same resistance. By contrast, for any given current I, $\bar{Q}_{irr,NMC}$ was larger at the working electrode made of 2D tape-casted NMC622 than at that made of 3D printed NMC622 with similar mass loading. This could be due to the fact that the electrical resistivity was larger and the lithium ion transport was slower in 2D tape-casted NMC622 than in 3D printed NMC622.

In fact, Fig. 7(b) plots the half-cell resistances estimated as $R_{ave,NMC} = \bar{Q}_{irr,NMC}/I^2$ and $R_{ave,Li} = \bar{Q}_{irr,Li}/I^2$ at constant C-rate. While the resistance $R_{ave,Li}$ of the lithium metal counter electrode was nearly the same between the two cells, the resistance $R_{ave,NMC}$ was larger for the half-cell with 2D tape-casted than that with 3D printed NMC622 working electrode. In addition, Fig. 7(c) plots the cell resistance R_{GC} calculated from the IR drop [Eq. (8)] in the calorimetric cells with working electrodes made of 3D printed or 2D tape-casted NMC622 at the end of the lithiation or delithiation steps during cycling at constant current I. Here also, the resistance R_{GC} of the cell with 2D tape-casted NMC622 was systematically larger than that with 3D printed NMC622. Both sets of independently obtained results were consistent, as the sum of half-cell resistances $R_{ave,NMC}$ and $R_{ave,Li}$ [Fig. 7(b)] was within the range of cell resistances $R_{GC,l}$ and $R_{GC,d}$ in lithiated or delithiated state [Fig. 7(c)].

4.3.5. Energy balance

Fig. 8 plots the specific net electrical energy loss $\Delta E_e/C_m$ [Eq. (6)] and the specific total thermal energy dissipated Q_T/C_m [Eq. (5)] per unit charge stored, as well as the predicted contributions from Joule heating Q_J/C_m and enthalpy of mixing Q_{mix}/C_m, averaged over the last three consecutive charging/discharging cycles for calorimetric cells with working electrodes made of (a) 3D printed or (b) 2D tape-casted NMC622 and lithium metal counter electrodes. Note that each term was divided by the specific capacity C_m of the cell to correct for any difference in mass loading. Here, for both cells at any given current I, the specific total dissipated thermal energy Q_T/C_m measured by *operando* isothermal calorimetry fell within experimental uncertainty of the specific net electrical energy loss $\Delta E_e/C_m$ measured by the potentiostat. In other words, the net electrical energy loss was entirely dissipated in the form of heat. These results confirm the accuracy of our measurements. As expected, the contributions of each energy dissipation mechanism increased with increasing C-rate in both cells. However, the cell with the 3D printed NMC622 electrode displayed 33% less thermal energy dissipation per unit charge stored than that with the 2D tape-casted NMC622 electrode. These results demonstrate that the novel 3D printing technology produced NMC622 electrodes with improved ionic transport and enhanced electronic transport resulting in superior specific capacity and significantly reduced heat generation. These features make 3D printed electrodes particularly attractive for fast charging applications, requiring less stringent thermal management to prevent thermal runaway, thus enhancing safety during operation.

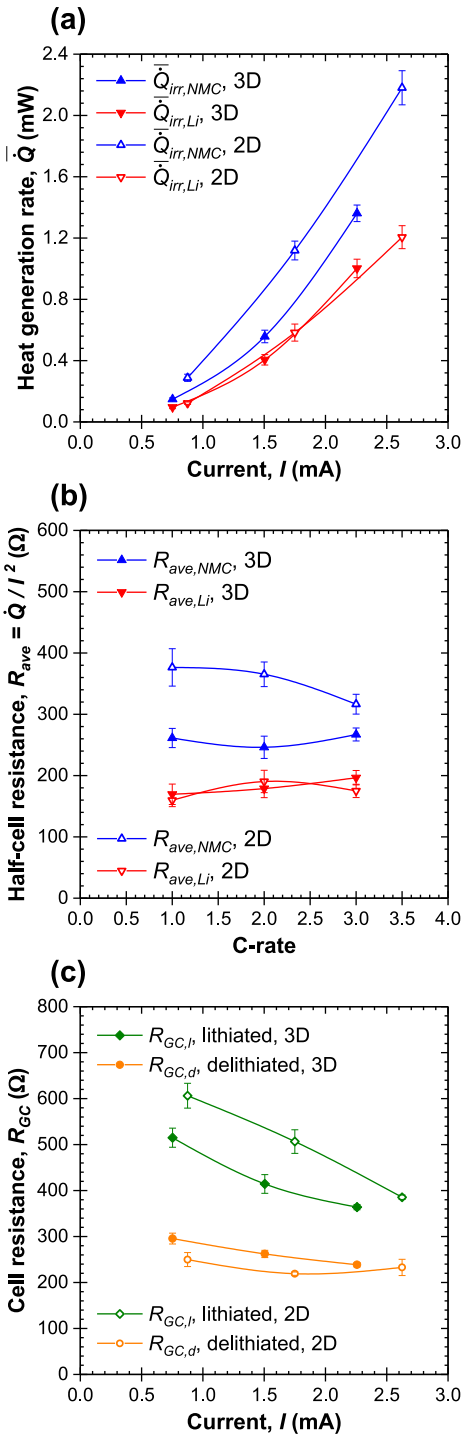

Fig. 7. (a) Time-averaged irreversible heat generation rates $\bar{Q}_{irr,NMC}$ and $\bar{Q}_{irr,Li}$ as functions of current I. (b) Half-cell resistances $R_{ave,NMC}$ and $R_{ave,Li}$ and (c) cell resistances $R_{GC,l}$ and $R_{GC,d}$ in lithiated or delithiated state [Eq. (8)] for calorimetric cells with working electrodes made of 3D printed or 2D tape-casted NMC622 under constant current cycling.

5. Conclusion

This study compares the thermodynamics behavior, ion transport, and energy dissipation in NMC622 electrodes made by a novel 3D printing technology with those made by the conventional 2D tape casting procedure. Potentiometric entropy measurements indicated that both types of electrodes had similar thermodynamics behavior. They both underwent lithium deintercalation in a homogeneous solid solution of NMC622 followed by a transition from a hexagonal (H1) phase to another hexagonal (H2) phase through a monoclinic (M) phase, as identified in other studies. *Operando* isothermal calorimetry revealed that, at high C-rates, the 3D printed electrodes exhibited larger specific capacity and better rate performance than the 2D tape-casted electrodes. This could be attributed to the larger electrode/electrolyte

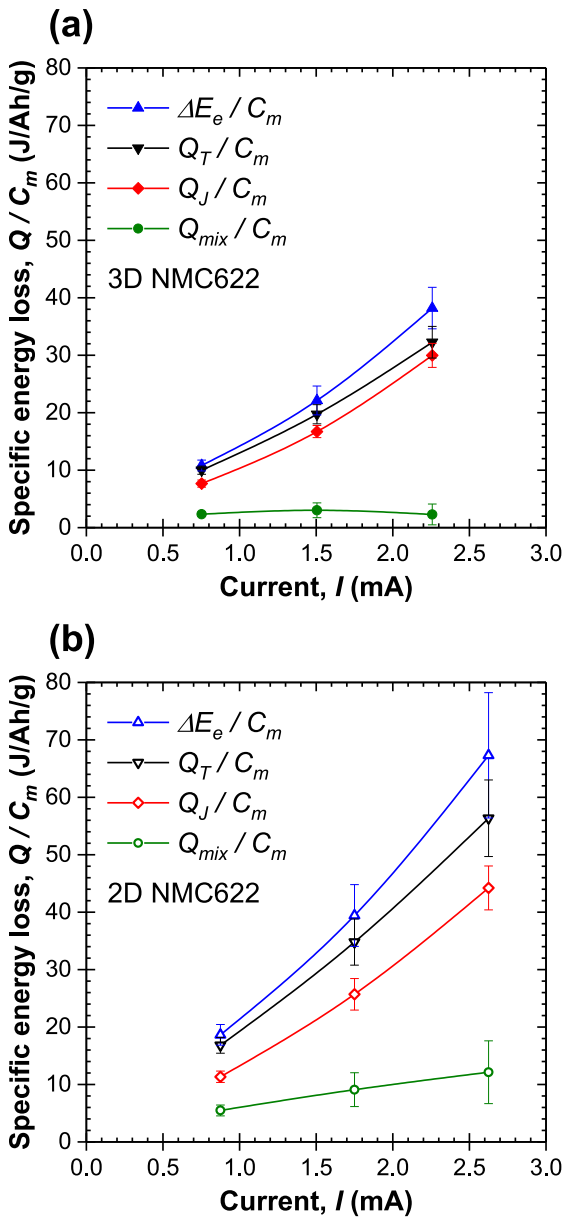

Fig. 8. Specific net electrical energy loss $\Delta E_e/C_m$ [Eq. (6)] and specific total thermal energy dissipated Q_T/C_m [Eq. (5)] per unit charge stored, as well as predicted contributions from Joule heating Q_J/C_m and enthalpy of mixing Q_{mix}/C_m, averaged over the last three consecutive charging/discharging cycles for calorimetric cells with working electrodes made of (a) 3D printed or (b) 2D tape-casted NMC622 and lithium metal counter electrodes.

interfacial surface area and electrical conductivity, and to the faster lithium ion transport in the 3D printed electrodes. These attributes also contributed to the smaller instantaneous heat generation rates and the reduced overall specific electrical energy and thermal energy dissipation per unit charge stored at the 3D printed electrodes than at the 2D tape-casted electrodes when tested under the same conditions. The superior electrochemical performance and the reduced heat generation of 3D printed NMC622 electrodes highlights the prospects of employing additive manufacturing techniques to create electrodes for fast charging batteries.

CRediT authorship contribution statement

Yucheng Zhou: Writing – review & editing, Writing – original draft, Visualization, Investigation, Formal analysis, Data curation, Conceptualization. **Asya Orhan:** Writing – review & editing, Investigation, Conceptualization. **Jianchao Ye:** Writing – review & editing, Investigation, Conceptualization. **Nicolas Leport:** Investigation, Conceptualization. **Marcus A. Worsley:** Supervision, Project administration, Funding acquisition. **Laurent Pilon:** Writing – review & editing, Supervision, Project administration, Funding acquisition, Conceptualization.

Declaration of competing interest

The authors declare that they have no known competing financial interests or personal relationships that could have appeared to influence the work reported in this paper.

Acknowledgments

This work was performed under the auspices of the U.S. Department of Energy by Lawrence Livermore National Laboratory under Contract DE-AC52-07NA27344 and was supported by the LLNL-LDRD program under project numbers 20-ERD-019 and 23-SI-002.

Appendix A. Supplementary data

Supplementary material related to this article can be found online at https://doi.org/10.1016/j.jpowsour.2024.235861.

Data availability

Data will be made available on request.

References

[1] A.K. Shukla, T.P. Kumar, Materials for next-generation lithium batteries, Current Sci. 94 (3) (2008) 314–331.
[2] J. Cao, A. Emadi, A new battery/ultracapacitor hybrid energy storage system for electric, hybrid, and plug-in hybrid electric vehicles, IEEE Trans. Power Electron. 27 (1) (2011) 122–132, http://dx.doi.org/10.1109/TPEL.2011.2151206.
[3] H. Kim, G. Jeong, Y.-U. Kim, J.-H. Kim, C.-M. Park, H.-J. Sohn, Metallic anodes for next generation secondary batteries, Chem. Soc. Rev. 42 (23) (2013) 9011–9034, http://dx.doi.org/10.1039/C3CS60177C.
[4] L. Lu, X. Han, J. Li, J. Hua, M. Ouyang, A review on the key issues for lithium-ion battery management in electric vehicles, J. Power Sources 226 (2013) 272–288, http://dx.doi.org/10.1016/j.jpowsour.2012.10.060.
[5] J. Zhang, L. Zhang, F. Sun, Z. Wang, An overview on thermal safety issues of lithium-ion batteries for electric vehicle application, IEEE Access 6 (2018) 23848–23863, http://dx.doi.org/10.1109/ACCESS.2018.2824838.
[6] M. Walter, M.V. Kovalenko, K.V. Kravchyk, Challenges and benefits of post-lithium-ion batteries, New J. Chem. 44 (5) (2020) 1677–1683, http://dx.doi.org/10.1039/C9NJ05682C.
[7] M. Toupin, T. Brousse, D. Belanger, Charge storage mechanism of MnO_2 electrode used in aqueous electrochemical capacitor, Chem. Mater. 16 (16) (2004) 3184–3190, http://dx.doi.org/10.1021/cm049649j.
[8] V. Augustyn, J. Come, M.A. Lowe, J.W. Kim, P.-L. Taberna, S.H. Tolbert, H.D. Abruna, P. Simon, B. Dunn, High-rate electrochemical energy storage through Li^+ intercalation pseudocapacitance, Nature Mater. 12 (6) (2013) 518–522, http://dx.doi.org/10.1038/nmat3601.
[9] V. Augustyn, P. Simon, B. Dunn, Pseudocapacitive oxide materials for high-rate electrochemical energy storage, Energy Environ. Sci. 7 (5) (2014) 1597–1614, http://dx.doi.org/10.1039/c3ee44164d.
[10] J. Come, V. Augustyn, J.W. Kim, P. Rozier, P.-L. Taberna, P. Gogotsi, J.W. Long, B. Dunn, P. Simon, Electrochemical kinetics of nanostructured Nb_2O_5 electrodes, J. Electrochem. Soc. 161 (5) (2014) A718–A725, http://dx.doi.org/10.1149/2.040405jes.
[11] M.R. Lukatskaya, B. Dunn, Y. Gogotsi, Multidimensional materials and device architectures for future hybrid energy storage, Nature Commun. 7 (1) (2016) 1–13, http://dx.doi.org/10.1038/ncomms12647.
[12] J.B. Cook, H.-S. Kim, T.C. Lin, C.-H. Lai, B. Dunn, S.H. Tolbert, Pseudocapacitive charge storage in thick composite MoS_2 nanocrystal-based electrodes, Adv. Energy Mater. 7 (2) (2017) 1601283, http://dx.doi.org/10.1002/aenm.201601283.

[13] Z. Fan, J. Yan, T. Wei, L. Zhi, G. Ning, T. Li, F. Wei, Asymmetric supercapacitors based on graphene/MnO_2 and activated carbon nanofiber electrodes with high power and energy density, Adv. Funct. Mater. 21 (12) (2011) 2366–2375, http://dx.doi.org/10.1002/adfm.201100058.

[14] F. Zhang, T. Zhang, X. Yang, L. Zhang, K. Leng, Y. Huang, Y. Chen, A high-performance supercapacitor-battery hybrid energy storage device based on graphene-enhanced electrode materials with ultrahigh energy density, Energy Environ. Sci. 6 (5) (2013) 1623–1632, http://dx.doi.org/10.1039/C3EE40509E.

[15] C. Choi, D.S. Ashby, D.M. Butts, R.H. DeBlock, Q. Wei, J. Lau, B. Dunn, Achieving high energy density and high power density with pseudocapacitive materials, Nat. Rev. Mater. 5 (1) (2020) 5–19, http://dx.doi.org/10.1038/s41578-019-0142-z.

[16] K. Ren, Z. Liu, T. Wei, Z. Fan, Recent developments of transition metal compounds-carbon hybrid electrodes for high energy/power supercapacitors, Nano-Micro Lett. 13 (1) (2021) 129, http://dx.doi.org/10.1007/s40820-021-00642-2.

[17] W. Wei, G. Oltean, C.-W. Tai, K. Edstrom, F. Bjorefors, L. Nyholm, High energy and power density TiO_2 nanotube electrodes for 3D Li-ion microbatteries, J. Mater. Chem. A 1 (28) (2013) 8160–8169, http://dx.doi.org/10.1039/C3TA11273J.

[18] J. Liu, C. Guan, C. Zhou, Z. Fan, Q. Ke, G. Zhang, C. Liu, J. Wang, A flexible quasi-solid-state nickel-zinc battery with high energy and power densities based on 3D electrode design, Adv. Mater. 28 (39) (2016) 8732–8739, http://dx.doi.org/10.1002/adma.201603038.

[19] Z. Du, D.L. Wood, C. Daniel, S. Kalnaus, J. Li, Understanding limiting factors in thick electrode performance as applied to high energy density Li-ion batteries, J. Appl. Electrochem. 47 (3) (2017) 405–415, http://dx.doi.org/10.1007/s10800-017-1047-4.

[20] J. Wang, Q. Sun, X. Gao, C. Wang, W. Li, F.B. Holness, M. Zheng, R. Li, A.D. Price, X. Sun, T.-K. Sham, X. Sun, Toward high areal energy and power density electrode for Li-ion batteries via optimized 3D printing approach, ACS Appl. Mater. Interfaces 10 (46) (2018) 39794–39801, http://dx.doi.org/10.1021/acsami.8b14797.

[21] X. Zhang, Z. Ju, Y. Zhu, K.J. Takeuchi, E.S. Takeuchi, A.C. Marschilok, G. Yu, Multiscale understanding and architecture design of high energy/power lithium-ion battery electrodes, Adv. Energy Mater. 11 (2) (2021) 2000808, http://dx.doi.org/10.1002/aenm.202000808.

[22] S. Chandrasekaran, D. Lin, Y. Li, M.A. Worsley, Aerogels, additive manufacturing, and energy storage, Joule 7 (5) (2023) 866–883, http://dx.doi.org/10.1016/j.joule.2023.03.021.

[23] K. Fu, Y. Wang, C. Yan, Y. Yao, Y. Chen, J. Dai, S. Lacey, Y. Wang, J. Wan, T. Li, Z. Wang, Y. Xu, L. Hu, Graphene oxide-based electrode inks for 3D-printed lithium-ion batteries, Adv. Mater. 28 (13) (2016) 2587–2594, http://dx.doi.org/10.1002/adma.201505391.

[24] C. Zhu, T. Liu, F. Qian, T.Y.-J. Han, E.B. Duoss, J.D. Kuntz, C.M. Spadaccini, M.A. Worsley, Y. Li, Supercapacitors based on three-dimensional hierarchical graphene aerogels with periodic macropores, Nano Lett. 16 (6) (2016) 3448–3456, http://dx.doi.org/10.1021/acs.nanolett.5b04965.

[25] B. Yao, S. Chandrasekaran, J. Zhang, W. Xiao, F. Qian, C. Zhu, E.B. Duoss, C.M. Spadaccini, M.A. Worsley, Y. Li, Efficient 3D printed pseudocapacitive electrodes with ultrahigh MnO_2 loading, Joule 3 (2) (2019) 459–470, http://dx.doi.org/10.1016/j.joule.2018.09.020.

[26] T. Roy, M.A. Salazar de Troya, M.A. Worsley, V.A. Beck, Topology optimization for the design of porous electrodes, Struct. Multidiscip. Optim. 65 (6) (2022) 171, http://dx.doi.org/10.1007/s00158-022-03249-2.

[27] X. Xue, D. Lin, Y. Li, Low tortuosity 3D-printed structures enhance reaction kinetics in electrochemical energy storage and electrocatalysis, Small Struct. 3 (12) (2022) 2200159, http://dx.doi.org/10.1002/sstr.202200159.

[28] M.D. Reale Batista, S. Chandrasekaran, B.D. Moran, M. Salazar de Troya, A. Pinongcos, Z. Wang, R. Hensleigh, A. Carleton, M. Zeng, T. Roy, D. Lin, X. Xue, V.A. Beck, D.A. Tortorelli, M. Stadermann, R. Zheng, Y. Li, M.A. Worsley, Design and additive manufacturing of optimized electrodes for energy storage applications, Carbon 205 (2023) 262–269, http://dx.doi.org/10.1016/j.carbon.2023.01.044.

[29] Y. Zhou, E. Le Calvez, S.W. Baek, M. Frajnkovič, C. Douard, E. Gautron, O. Crosnier, T. Brousse, L. Pilon, Effect of particle size on thermodynamics and lithium ion transport in electrodes made of $Ti_2Nb_2O_9$ microparticles or nanoparticles, Energy Storage Mater. 52 (2022) 371–385, http://dx.doi.org/10.1016/j.ensm.2022.08.010.

[30] S.W. Baek, K.E. Wyckoff, D.M. Butts, J. Bienz, A. Likitchatchawankun, M.B. Preefer, M. Frajnkovič, B.S. Dunn, R. Seshadri, L. Pilon, *Operando* calorimetry informs the origin of rapid rate performance in microwave-prepared $TiNb_2O_7$ electrodes, J. Power Sources 490 (2021) 229537, http://dx.doi.org/10.1016/j.jpowsour.2021.229537.

[31] S.W. Baek, M.B. Preefer, M. Saber, K. Zhai, M. Frajnkovič, Y. Zhou, B.S. Dunn, A.V. der Ven, R. Seshadri, L. Pilon, Potentiometric entropy and *operando* calorimetric measurements reveal fast charging mechanisms in PNb_9O_{25}, J. Power Sources 520 (2022) 230776, http://dx.doi.org/10.1016/j.jpowsour.2021.230776.

[32] S.W. Baek, K.E. Wyckoff, D.D. Robertson, M. Frajnkovič, Y. Zhou, S.H. Tolbert, R. Seshadri, L. Pilon, *Operando* calorimetry investigation of particle size effects on heat generation in Wadsley-Roth $(W_{0.2}V_{0.8})_3O_7$-based electrodes, ACS Appl. Energy Mater. 6 (3) (2023) 1355–1367, http://dx.doi.org/10.1021/acsaem.2c03150.

[33] K.R. Tallman, G.P. Wheeler, C.J. Kern, E. Stavitski, X. Tong, K.J. Takeuchi, A.C. Marschilok, D.C. Bock, E.S. Takeuchi, Nickel-rich nickel manganese cobalt (NMC622) cathode lithiation mechanism and extended cycling effects using *operando* X-ray absorption spectroscopy, J. Phys. Chem. C 125 (1) (2021) 58–73, http://dx.doi.org/10.1021/acs.jpcc.0c08095.

[34] X. Wang, H. Zhou, Z. Chen, X. Meng, Synchrotron-based X-ray diffraction and absorption spectroscopy studies on layered $LiNi_xMn_yCo_zO_2$ cathode materials: A review, Energy Storage Mater. 49 (2022) 181–208, http://dx.doi.org/10.1016/j.ensm.2022.04.012.

[35] M. Drews, S. Tepner, P. Haberzettl, H. Gentischer, W. Beichel, M. Breitwieser, S. Vierrath, D. Biro, Towards 3D-lithium ion microbatteries based on silicon/graphite blend anodes using a dispenser printing technique, RSC Adv. 10 (38) (2020) 22440–22448, http://dx.doi.org/10.1039/D0RA03161E.

[36] J. Zhao, Y. Zhang, X. Zhao, R. Wang, J. Xie, C. Yang, J. Wang, Q. Zhang, L. Li, C. Lu, Y. Yao, Direct ink writing of adjustable electrochemical energy storage device with high gravimetric energy densities, Adv. Funct. Mater. 29 (26) (2019) 1900809, http://dx.doi.org/10.1002/adfm.201900809.

[37] C. Zhu, N.B. Schorr, Z. Qi, B.R. Wygant, D.E. Turney, G.G. Yadav, M.A. Worsley, E.B. Duoss, S. Banerjee, E.D. Spoerke, A. van Buuren, T.N. Lambert, Direct ink writing of 3D Zn structures as high-capacity anodes for rechargeable alkaline batteries, Small Struct. 4 (4) (2023) 2200323, http://dx.doi.org/10.1002/sstr.202200323.

[38] B. Yao, H. Peng, H. Zhang, J. Kang, C. Zhu, G. Delgado, D. Byrne, S. Faulkner, M. Freyman, X. Lu, M.A. Worsley, J.Q. Lu, Y. Li, Printing porous carbon aerogels for low temperature supercapacitors, Nano Lett. 21 (9) (2021) 3731–3737, http://dx.doi.org/10.1021/acs.nanolett.0c04780.

[39] M. Idrees, S. Batool, J. Cao, M.S. Javed, S. Xiong, C. Liu, Z. Chen, 3D printed PC/SiOC@Zn hybrid composite as dendrite-free anode for Zn-ion battery, Nano Energy 100 (2022) 107505, http://dx.doi.org/10.1016/j.nanoen.2022.107505.

[40] E. Brown, P. Yan, H. Tekik, A. Elangovan, J. Wang, D. Lin, J. Li, 3D printing of hybrid MoS_2-graphene aerogels as highly porous electrode materials for sodium ion battery anodes, Mater. Des. 170 (2019) 107689, http://dx.doi.org/10.1016/j.matdes.2019.107689.

[41] B. Yao, S. Chandrasekaran, H. Zhang, A. Ma, J. Kang, L. Zhang, X. Lu, F. Qian, C. Zhu, E.B. Duoss, C.M. Spadaccini, M.A. Worsley, Y. Li, 3D-printed structure boosts the kinetics and intrinsic capacitance of pseudocapacitive graphene aerogels, Adv. Mater. 32 (8) (2020) 1906652, http://dx.doi.org/10.1002/adma.201906652.

[42] D. Lin, S. Chandrasekaran, J.-B. Forien, X. Xue, A. Pinongcos, E. Coester, M.A. Worsley, Y. Li, 3D-printed graded electrode with ultrahigh MnO_2 loading for non-aqueous electrochemical energy storage, Adv. Energy Mater. 13 (20) (2023) 2300408, http://dx.doi.org/10.1002/aenm.202300408.

[43] C. Chen, J. Jiang, W. He, W. Lei, Q. Hao, X. Zhang, 3D printed high-loading lithium-sulfur battery toward wearable energy storage, Adv. Funct. Mater. 30 (10) (2020) 1909469, http://dx.doi.org/10.1002/adfm.201909469.

[44] K. Shen, B. Li, S. Yang, 3D printing dendrite-free lithium anodes based on the nucleated MXene arrays, Energy Storage Mater. 24 (2020) 670–675, http://dx.doi.org/10.1016/j.ensm.2019.08.015.

[45] H. Yang, H. Wang, W. Li, B. Tian, T. Xu, D. Kong, S. Huang, K. Liu, X. Li, H.Y. Yang, Y. Wang, A simple and effective host for sodium metal anode: a 3D-printed high pyrrolic-N doped graphene microlattice aerogel, J. Mater. Chem. A 10 (32) (2022) 16842–16852, http://dx.doi.org/10.1039/D2TA03294E.

[46] L. Zeng, H. He, H. Chen, D. Luo, J. He, C. Zhang, 3D printing architecting reservoir-integrated anode for dendrite-free, safe, and durable Zn batteries, Adv. Energy Mater. 12 (12) (2022) 2103708, http://dx.doi.org/10.1002/aenm.202103708.

[47] A.C. Martinez, A. Maurel, A.P. Aranzola, S. Grugeon, S. Panier, L. Dupont, J.A. Hernandez-Viezcas, B. Mummareddy, B.L. Armstrong, P. Cortes, S.T. Sreenivasan, E. MacDonald, Additive manufacturing of $LiNi_1/3Mn_1/3Co_{1/3}O_2$ battery electrode material via vat photopolymerization precursor approach, Sci. Rep. 12 (1) (2022) 19010, http://dx.doi.org/10.1038/s41598-022-22444-1.

[48] R. Tao, Y. Gu, J. Sharma, K. Hong, J. Li, A conformal heat-drying direct ink writing 3D printing for high-performance lithium-ion batteries, Mater. Today Chem. 32 (2023) 101672, http://dx.doi.org/10.1016/j.mtchem.2023.101672.

[49] S.W. Baek, M. Saber, A. Van der Ven, L. Pilon, Thermodynamic analysis and interpretative guide to entropic potential measurements of lithium-ion battery electrodes, J. Phys. Chem. C 126 (14) (2022) 6096–6110, http://dx.doi.org/10.1021/acs.jpcc.1c10414.

[50] W. Weppner, R.A. Huggins, Determination of the kinetic parameters of mixed-conducting electrodes and application to the system Li_3Sb, J. Electrochem. Soc. 124 (10) (1977) 1569–1578, http://dx.doi.org/10.1149/1.2133112.

[51] J. Newman, K.E. Thomas, H. Hafezi, D.R. Wheeler, Modeling of lithium-ion batteries, J. Power Sources 119 (2003) 838–843, http://dx.doi.org/10.1016/S0378-7753(03)00282-9.

[52] K.E. Thomas, J. Newman, Thermal modeling of porous insertion electrodes, J. Electrochem. Soc. 150 (2) (2003) A176–A192, http://dx.doi.org/10.1149/1.1531194.

[53] G. Liu, M. Ouyang, L. Lu, J. Li, X. Han, Analysis of the heat generation of lithium-ion battery during charging and discharging considering different influencing factors, J. Therm. Anal. Calorim. 116 (2) (2014) 1001–1010, http://dx.doi.org/10.1007/s10973-013-3599-9.

[54] G. Assat, S.L. Glazier, C. Delacourt, J.-M. Tarascon, Probing the thermal effects of voltage hysteresis in anionic redox-based lithium-rich cathodes using isothermal calorimetry, Nat. Energy 4 (8) (2019) 647–656, http://dx.doi.org/10.1038/s41560-019-0410-6.

[55] K.E. Thomas, J. Newman, Heats of mixing and of entropy in porous insertion electrodes, J. Power Sources 119 (2003) 844–849, http://dx.doi.org/10.1016/S0378-7753(03)00283-0.

[56] K. Smith, C.-Y. Wang, Power and thermal characterization of a lithium-ion battery pack for hybrid-electric vehicles, J. Power Sources 160 (1) (2006) 662–673, http://dx.doi.org/10.1016/j.jpowsour.2006.01.038.

[57] A.V. der Ven, K.A. See, L. Pilon, Hysteresis in electrochemical systems, Battery Energy 1 (2) (2022) 20210017, http://dx.doi.org/10.1002/bte2.20210017.

[58] A. Burke, M. Miller, Testing of electrochemical capacitors: Capacitance, resistance, energy density, and power capability, Electrochim. Acta 55 (25) (2010) 7538–7548, http://dx.doi.org/10.1016/j.electacta.2010.04.074.

[59] M.D. Stoller, R.S. Ruoff, Best practice methods for determining an electrode material's performance for ultracapacitors, Energy Environ. Sci. 3 (9) (2010) 1294–1301, http://dx.doi.org/10.1039/c0ee00074d.

[60] S. Zhao, F. Wu, L. Yang, L. Gao, A.F. Burke, A measurement method for determination of dc internal resistance of batteries and supercapacitors, Electrochem. Commun. 12 (2) (2010) 242–245, http://dx.doi.org/10.1016/j.elecom.2009.12.004.

[61] B.-A. Mei, O. Munteshari, J. Lau, B. Dunn, L. Pilon, Physical interpretations of Nyquist plots for EDLC electrodes and devices, J. Phys. Chem. C 122 (1) (2018) 194–206, http://dx.doi.org/10.1021/acs.jpcc.7b10582.

[62] O. Munteshari, J. Lau, D.S. Ashby, B. Dunn, L. Pilon, Effects of constituent materials on heat generation in individual EDLC electrodes, J. Electrochem. Soc. 165 (7) (2018) A1547–A1557, http://dx.doi.org/10.1149/2.0771807jes.

[63] N.S. Hudak, L.E. Davis, G. Nagasubramanian, Cycling-induced changes in the entropy profiles of lithium cobalt oxide electrodes, J. Electrochem. Soc. 162 (3) (2015) A315–A321, http://dx.doi.org/10.1149/2.0071503jes.

[64] S. Ma, M. Jiang, P. Tao, C. Song, J. Wu, J. Wang, T. Deng, W. Shang, Temperature effect and thermal impact in lithium-ion batteries: A review, Progr. Nat. Sci.: Mater. Int. 28 (6) (2018) 653–666, http://dx.doi.org/10.1016/j.pnsc.2018.11.002.

[65] H.Y. Alolaywi, K. Uzun, Y.-T. Cheng, "Zero" porosity high loading NMC622 positive electrodes for Li-ion batteries, J. Electrochem. Soc. 171 (1) (2024) 010514, http://dx.doi.org/10.1149/1945-7111/ad1a20.